



# Molten-salt assisted synthesis of polymeric carbon nitride-based photocatalyst for enhanced photocatalytic activity under green light irradiation

Chengqun Xu<sup>a,\*</sup>, Haiyang Liu<sup>a</sup>, Dongyu Wang<sup>a</sup>, Dezhi Li<sup>a</sup>, Ying Zhang<sup>d</sup>, Xiaolu Liu<sup>b</sup>, Jingyao Huang<sup>a</sup>, Shengquan Wu<sup>a</sup>, Donghua Fan<sup>a</sup>, Hongguang Liu<sup>d,a,\*\*</sup>, Hui Pan<sup>b,c,\*\*\*</sup>

<sup>a</sup> School of Applied Physics and Materials, Wuyi University, Jiangmen 529020, PR China

<sup>b</sup> Institute of Applied Physics and Materials Engineering, University of Macau, Macao SAR, 999078, P. R. China

<sup>c</sup> Department of Physics and Chemistry, Faculty of Science and Technology, University of Macau, Macao SAR, 999078, P. R. China

<sup>d</sup> College of Chemistry and Materials Science, Jinan University, 601 Huang-Pu Avenue West, Guangzhou 510632, PR China

## ARTICLE INFO

### Keywords:

PCN  
Ionothermal method  
NaCl-KCl  
Aminobenzonitrile  
Green light

## ABSTRACT

The co-condensation of dicyandiamide and aminobenzonitrile (ABN) followed by post-calcination in NaCl-KCl molten salt can endow the Polymeric Carbon Nitride (PCN) with enhanced electron delocalization and defects ( $\text{C}\equiv\text{N}$  and nitrogen defects), leading to extended optical absorption range and improved separation rate of photogenerated carriers. As a consequence, the active-optimized DCN-NaK-90ABN accounts for 76 times promotion than DCN in photodegradation of bisphenol A (BPA) under visible light. More importantly, the photocatalytic activity is demonstrated by the significantly enhanced degradation of BPA and  $\text{H}_2$  production under  $\lambda > 500$  nm, which are much better than those of most previously reported PCN-based photocatalysts. Furthermore, the theoretical calculations certify the validity of proposed structure and explain the reactive mechanism combining with the experimental results. Our findings shed light on a new pathway for designing the efficient photocatalysts to capture the long wavelength solar power.

## 1. Introduction

Recently, polymeric carbon nitride (PCN), as a metal-free photocatalyst, has attracted intensive interest due to the potential applications in  $\text{CO}_2$  reduction, degradation of organic pollutants, water splitting, etc [1–5]. As the lowest unoccupied molecular orbital (LUMO) is contributed by the C 2p and N 2p orbitals, while the highest occupied molecular orbital (HOMO) is mainly located on the N 2p orbitals [6], the overlapped N 2p orbitals in pristine PCN lead to the low delocalization of  $\pi$ -electron accompanying with the restricted optical absorption range (no more than 460 nm) and high charge carrier recombination rate. Therefore, the photocatalytic activity of pristine PCN is poor under the visible light irradiation. Various strategies have been proposed to optimize the electronic structures of PCN, such as construction of heterojunction, doping, and modification of microstructure [7–11].

Recently, a molten salts (MS)-based strategy, where the salts act as

both of solvent and template, has been adopted to modulate the electronic structure and properties of PCN [12–14]. Bojdys et al. first reported the polycondensation of melamine in the KCl-LiCl molten salts, demonstrating the significant improvement of crystallinity and specific surface area for PCN [15]. Highly crystalline species with shrinkable  $\pi$ - $\pi$  layer stacking distance were obtained by post-calcinating the co-condensation of oxamide and urea in KCl-LiCl molten salts, promoting the interlayer exciton dissociation and lateral charge transportation. Finally, the photocatalytic hydrogen evolution (PHE) performance was notably improved [16]. Previous studies mainly focused on the KCl-LiCl molten salts [17,18]. The melting point (mp) of KCl-LiCl eutectic salts is 352 °C, which is inferior to the typical polymerization temperature of PCN (550 °C). Therefore, the KCl-LiCl eutectic salts can act as a strong monomer solvation as well as inert liquid environment to promote the crystallinity of PCN. However, the inactive triazine-based motif [poly (triazine imide), PTI] as major component was generated in the presence

\* Corresponding author.

\*\* Corresponding author at: College of Chemistry and Materials Science, Jinan University, 601 Huang-Pu Avenue West, Guangzhou 510632, PR China.

\*\*\* Corresponding author at: Institute of Applied Physics and Materials Engineering, University of Macau, Macao SAR, 999078, P. R. China.

E-mail addresses: [xuchengqun2019@yeah.net](mailto:xuchengqun2019@yeah.net) (C. Xu), [hongguang\\_liu@jnu.edu.cn](mailto:hongguang_liu@jnu.edu.cn) (H. Liu), [huippan@um.edu.mo](mailto:huippan@um.edu.mo) (H. Pan).

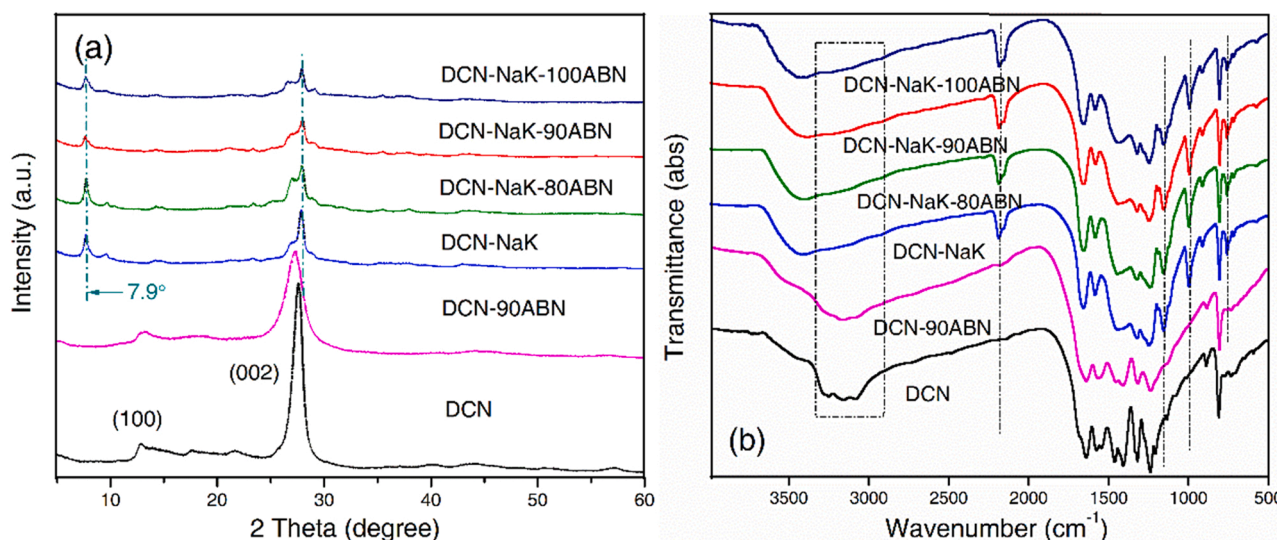


Fig. 1. (a) Powder XRD patterns and (b) FT-IR spectra of DCN, DCN-90ABN, DCN-NaK and DCN-NaK-xABN.

of lithium, which limits the photocatalytic activity [19,20]. Wang' group used a two-step thermal polymerization to decrease the content of PTI, that is, pre-heating melamine to obtain the active intermediate tri-s-triazine-based motif and then calcinating the intermediate in the KCl-LiCl eutectic salts. The as-obtained samples exhibited high crystallinity and excellent activity toward hydrogen evolution [21]. Furthermore, the alternative MS (NaCl-KCl) with different mp (650 °C) and absence of lithium were explored [22]. The high mp of NaCl-KCl in the absence of lithium may only partially "dissolve" the PCN and promote the generation of tri-s-triazine, significantly improving the water splitting into H<sub>2</sub> [23]. Although the PHE performance was obviously enhanced by the ionothermal method, two essential questions are still rarely explored: i) the improvement of photocatalytic activity is limited to the irradiation of less than 460 nm and that under longer wavelength illumination is still low, and ii) the photodegradation of PCN with oxidation ability for organic pollutions is rarely reported.

Considering the pristine PCN, engineering its molecular structure is feasible for expanding the optical response range by the route of organic chemistry [24,25], which had been demonstrated in our previous works, such as the enhanced delocalization by the incorporation of 1,3,5-tris (4-aminophenyl)benzene [26], the construction of D-A structure by the fusion of acetylacetone [27], the coordination of D-A structure and the delocalization by the grafted thiophene-2,5-dicarbaldehyde [28].

Herein, the graft of aminobenzonitrile (ABN) and NaCl-KCl molten salts were adopted to optimize the structure of PCN by a two-step thermal polymerization. We find that the optical absorption range is extended and the recombination of photogenerated carriers is suppressed by the enhanced delocalization and the formational defect-containing ( $-C\equiv N$  and nitrogen defect) in PCN, which are confirmed by the density functional theory (DFT) calculations. The as-prepared samples exhibit significantly enhanced activity for PHE and photodegradation of BPA, especially at the irradiations of 500 and 550 nm.

## 2. Experimental details

### 2.1. Synthesis procedure

4.0 g of dicyandiamide and a designed amount of aminobenzonitrile (ABN) were mixed homogeneously. Then the mixture was moved to 100 mL of alumina crucible with a lid and calcined at 500 °C for 2 h in a muffle furnace. The related polymerization route was shown in Scheme S1. The obtained solid powder and 6.0 g of metal salts (4.28 g NaCl and 1.72 g KCl) were ground for 20 min to promote the uniform mixing. The

mixture was calcinated at 610 °C for 2 h in oven with the flow of N<sub>2</sub>. The final product was thoroughly washed with deionized water (DI) to remove excess amounts of salts and dried in vacuum oven. The products were labeled as DCN-NaK-xABN (x = 80, 90, 100 mg). DCN-NaK and DCN-90ABN were prepared using a similar procedure without adding ABN and the metal salts, respectively. DCN was also obtained under similar conditions except for the addition of ABN and the metal salts.

### 2.2. Characterizations

The crystal structures of the prepared samples were recorded by an X-ray diffraction (XRD, Bruker D8 advance diffractometer with Cu-radiation) and Fourier transform infrared (FTIR, PerkinElmer spectrometer) spectroscopy. X-ray photoelectron spectroscopy (XPS, Thermo Scientific ESCALAB 250) and Elemental analysis (VARIO EL CUBE microanalyzer) were adopted to investigate the chemical states and elemental composition. The morphology and microstructure were collected by JEM-2100 F transmission electron microscope (TEM) and Hitachi SU 8220 scanning electron microscope (SEM). UV-vis diffuse reflectance spectra (UV-vis DRS) were measured on a UV-3600 plus UV-vis-NIR spectrophotometer with BaSO<sub>4</sub> as a reference. The solid-state <sup>13</sup>C NMR was recorded by a JEOL ECA500 spectrometer. BET surface areas and N<sub>2</sub> adsorption-desorption isotherms were collected by Micromeritics TriStar II 3020. Electron paramagnetic resonance (EPR) spectra (JEOL JES FA200 spectrometer) were analyzed to detect the active species in the photodegradation of BPA. Photoluminescence (PL) spectra were obtained on a fluorescence spectrophotometer (FLS-980) at room temperature. Moreover, electrochemical measurement was performed using a three-electrode quartz cell on a CHI 660 C electrochemical workstation (Shanghai Chenhua, China). The detailed information was provided in the Supporting Information. Electronic band structures of DCN and DCN-NaK-xABN were calculated based on the density-functional theory (DFT) that was carried out using the Perdew-Burke-Ernzerhof (PBE) functional and plane-wave ultrasoft pseudopotential implemented in the CASTEP code [29,30]. The related discussions were described in the Supporting Information.

### 2.3. Photocatalytic tests

#### 2.3.1. Photodegradation of BPA

The photodegradation of BPA over the as-prepared samples (DCN, DCN-NaK, DCN-90ABN and DCN-NaK-xABN) were carried out to evaluate the photocatalytic activity under different wavelength

illumination. In detail, 50 mg of catalyst was dispersed into the BPA aqueous solution (100 mL, 20 mg/L) and continuously stirred for 60 min in dark condition. The system was exposed to the illumination of 300 W Xe-lamp (PLS-SXE300D, Beijing Perfectlight Technology Co., Ltd) with 420 nm cutoff filter, and 500 nm and 550 nm bandpass filter, respectively. Then 2 mL of reaction solution was taken out at regular time intervals and filtered through a 0.45  $\mu\text{m}$  of membrane. Moreover, for detecting the active species in the photodegradation process, tert-butyl alcohol (500  $\mu\text{L}$ , TBA), and triethanolamine (500  $\mu\text{L}$ , TEA) and  $\text{N}_2$  gas flow were introduced into the solution as the scavengers of hydroxyl radicals ( $\cdot\text{OH}$ ), positive holes ( $\text{h}^+$ ) and dissolved  $\text{O}_2$ , respectively. The reaction solution was monitored by a high-performance liquid chromatography system (HPLC, Waters e2695 Alliance) with a fluorescence detector at 254 nm.

### 2.3.2. Photocatalytic hydrogen evolution (PHE)

The PHE performance was examined by PerfectLight Labsolar-6A full glass automatic online trace gas analysis system equipped with a Fuli GC9790SD gas chromatography. The reaction solution was prepared as follows: 50 mg of catalyst was dispersed into the 100 mL of mixed solution (10 mL of TEA, 3 wt% of Pt from dissolved  $\text{H}_2\text{PtCl}_6 \cdot 6\text{H}_2\text{O}$  (5 mL) and 85 mL of deionized water). Then reaction was carried out in a Pyrex top-irradiation reaction vessel connected to a glass closed gas circulation system. The solution was degassed for 30 min to remove air prior to illumination under a 300 W Xe-lamp (PLS-SXE300D, Beijing Perfectlight Technology Co., Ltd) equipped with a 420 nm cutoff filter, and 500 nm and 550 nm bandpass filters, respectively. The apparent quantum efficiency (AQE) was estimated according to the following Eq. (1) and our previous work [27]:

$$\text{AQE}(\%) = \frac{2 \times \text{number of evolved } \text{H}_2 \text{ molecules}}{\text{number of incident photons}} \times 100 \quad (1)$$

## 3. Results and discussion

### 3.1. Phase structure, morphology, and surface chemical state

The crystal structures of DCN, DCN-90ABN, DCN-NaK and DCN-NaK-xABN were demonstrated by the X-ray diffraction (XRD) patterns (Fig. 1a). All the samples show two typical characteristic peaks of PCN related to the (100) and (002) crystal planes, corresponding to the interplanar packing and interlayer-stacking of heptazine, respectively [31]. The (002) peak is shifted from  $27.6^\circ$  for DCN to  $27.3^\circ$  for DCN-90ABN. Meanwhile, the interlayer-stacking peak becomes weaker and broader gradually with the increased content of ABN in DCN-NaK-xABN, indicating the interlayer-stacking order of PCN is disrupted with the incorporation of ABN into the CN networks during the thermal polymerization process. Furthermore, the peak positions of (100) and (002) change obviously as molten salts was used. The (100) peak moves down from  $12.9^\circ$  with an in-plane repeated unit of 0.688 nm for DCN to  $7.9^\circ$  with a repeated unit of 1.125 nm for DCN-NaK and DCN-NaK-xABN, because the large ions (K and Na) are introduced into the heptazine units and then enlarge the packing distance [32]. The (002) peak at  $27.6^\circ$  that corresponds to an interlayer distance of 0.323 nm for DCN shifts up to  $28.0^\circ$  (distance = 0.318 nm), indicating the decreased interlayer distance by the treatment of molten salt. The compacted interlayer-stacking in DCN-NaK and DCN-NaK-xABN can promote charge and energy transportation within the layers, which would be beneficial to the photocatalytic activity [16,33]. No characteristic peaks of NaCl and KCl crystals can be found, suggested complete elimination of the salts by the washing treatment in boiled water. The FTIR spectra of the as-prepared samples were collected to characterize the molecular structures (Fig. 1b). DCN and DCN-90ABN exhibit almost the same characteristic peaks. A typical peak at  $810\text{ cm}^{-1}$  belongs to the out-of-plane bending mode of heptazine rings, while the fingerprint located between  $1200$  and  $1800\text{ cm}^{-1}$  are the breathing modes of CN

**Table 1**

Elemental Composition and the BET Specific Surface Area of DCN, DCN-90ABN, DCN-NaK and DCN-NaK-xABN.

Sample	N% (wt%)	C% (wt%)	C/N	$S_{\text{BET}}$ ( $\text{m}^2/\text{g}$ )
DCN	61.24	34.76	0.662	23.1
DCN-90ABN	59.22	34.75	0.685	7.4
DCN-NaK	43.68	26.42	0.706	17.0
DCN-NaK-80ABN	43.06	26.40	0.715	37.2
DCN-NaK-90ABN	41.47	25.74	0.724	34.1
DCN-NaK-100ABN	41.41	25.72	0.725	17.4

heterocycles. The broad peaks in the range from  $3000$  to  $3600\text{ cm}^{-1}$  are originated from the stretching vibration of terminal amino groups (N-H) and adsorbed water (O-H) [34]. With the use of NaCl-KCl, the peak intensity of DCN-NaK and DCN-NaK-xABN between  $3000$  and  $3300\text{ cm}^{-1}$  exhibits a significant decrease, which can be attributed to the loss of N-H stretching. Furthermore, an obvious peak for DCN-NaK and DCN-NaK-xABN appears in  $2181\text{ cm}^{-1}$ , originating from the stretching vibration of cyano groups ( $\text{C}\equiv\text{N}$ ) [17,35] because of the partial loss of amine groups in heptazine rings under high temperature in eutectic NaCl-KCl salt [21,36]. Two new absorption bands at  $992$  and  $1154\text{ cm}^{-1}$  for DCN-NaK and DCN-NaK-xABN can be assigned to the symmetric and asymmetric vibrations of  $\text{NC}_2$  bonds, respectively, in metal- $\text{NC}_2$  groups [16,37], which further confirm the above XRD results that the ions (K and Na) are introduced into the heptazine units. A weak peak at around  $756\text{ cm}^{-1}$  can be detected due to the existence of low content PTI (C-NH-C bending vibrations) [12]. In addition, the similar FTIR spectra among the as-prepared samples suggest the core frame structure of PCN is well maintained even though undergoing the incorporation of ABN and the ionothermal method.

Elemental analysis (EA) clearly discloses the compositional variation of the samples (Table 1). The C/N molar ratio of DCN is 0.662, whereas that of DCN-90ABN increases to 0.685, indicating the increased C content accompanying with the fusion of ABN in the CN framework. The C/N molar ratio of DCN-NaK (0.706) is much higher than that of DCN because of the generation of nitrogen defects after heating in the molten salts environment, which is consistent with the results of decreased amine groups in FTIR. Furthermore, the C/N molar ratio is further increased gradually as the ABN content in the DCN-NaK-xABN increases, certifying the incorporation of ABN into the CN network.

In order to certify the effect of nitrogen defects, EPR analysis were adopted (Fig. S1, Supporting Information). A weak symmetrical resonance signal at  $g = 2.003$  for DCN could be observed in dark, indicating the existence of nitrogen defects in PCN during the high-temperature condensation process [31,34]. With the incorporation of TAP and the treatment of NaCl-KCl molten salts, a strong analogous resonance signal for DCN-NaK-90ABN appeared, indicating the increased content of nitrogen defects. Furthermore, after visible light irradiation, the EPR intensity of DCN-NaK-90ABN was much higher than that of DCN, which can be ascribed to the efficient photochemical generation of radicals in DCN-NaK-90ABN and is favorable to the photocatalytic activity [38].

X-ray photoelectron spectroscopy (XPS) shows that C, N, O, Na and K are observed in DCN-NaK-90ABN and DCN-NaK (Fig. S2a, Supporting Information). No Cl signal appears in the XPS survey because of the emission of HCl or/and  $\text{NH}_4\text{Cl}$  ( $\text{NH}_3 + \text{HCl} \rightarrow \text{NH}_4\text{Cl}$ ) at high temperature [7]. The high-resolution N 1s spectrum of DCN consists of three peaks,  $\text{sp}^2\text{-C-N} = \text{C}$  ( $398.7\text{ eV}$ ),  $\text{N-(C)}_3$  ( $399.4\text{ eV}$ ) and  $\text{C-N-H}_x$  ( $401.2\text{ eV}$ ) (Fig. 2a). The peak area ratio of  $\text{N}_{(\text{C-N-C})}/\text{N}_{(\text{N-(C)}_3)}$  is from 1.40 for DCN to 0.82 for DCN-NaK and 0.88 for DCN-NaK-90ABN, respectively, indicating the generated nitrogen defects (Table 1) are mainly originated from the missing  $\text{C-N} = \text{C}$  lattice sites in the thermal polymerization process. Interestingly, the peak area ratio of  $\text{N}_{(\text{C-N-H}_x)}/\text{N}_{(\text{N-(C)}_3)}$  is increased from 0.18 for DCN to 0.30 for DCN-NaK and 0.24 for DCN-NaK-90ABN, respectively, which can be attributed to the formation of cyano group ( $\text{C}\equiv\text{N}$ ) [18,36]. The C 1s and K 2p spectra (Fig. 2b)



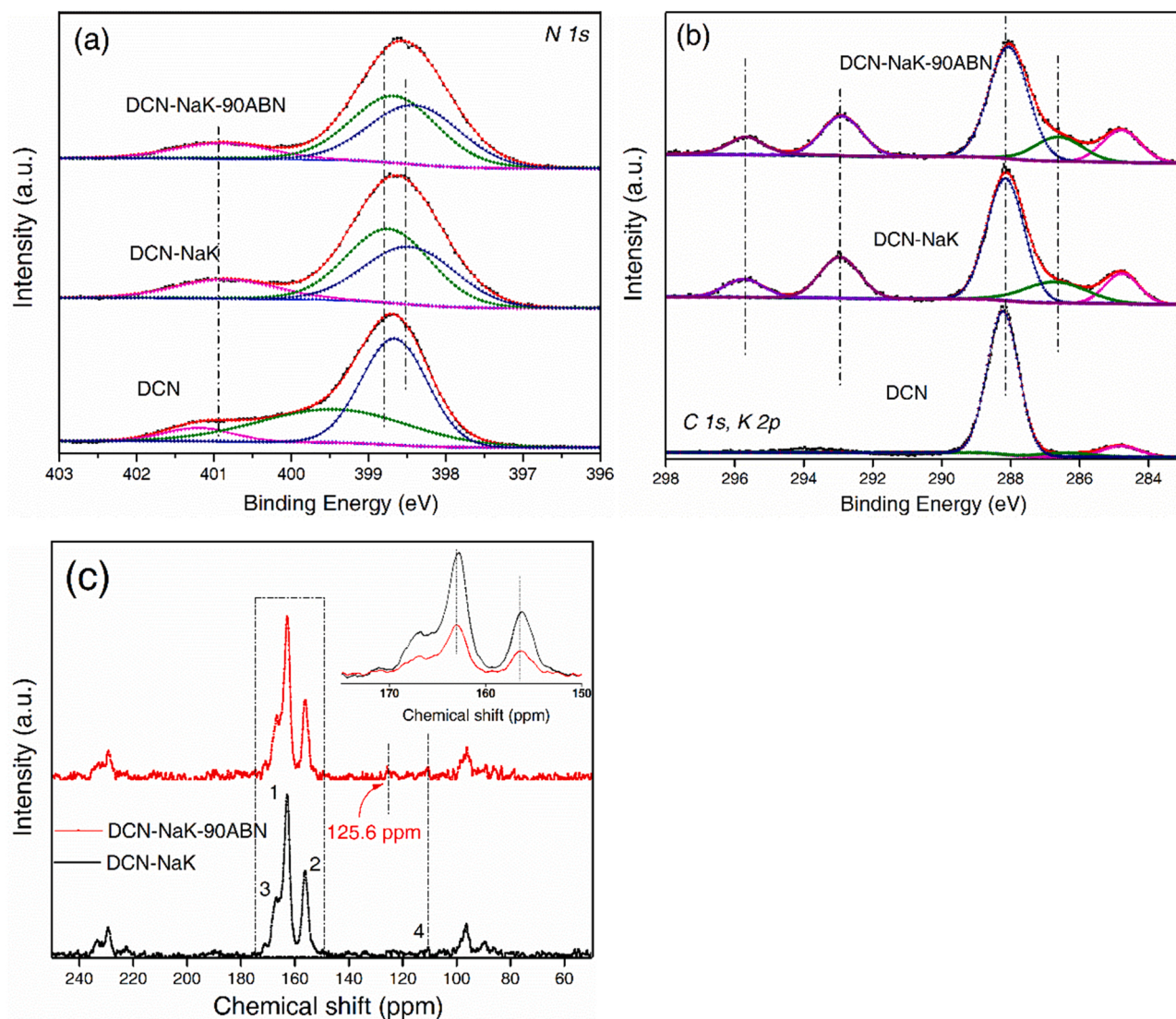
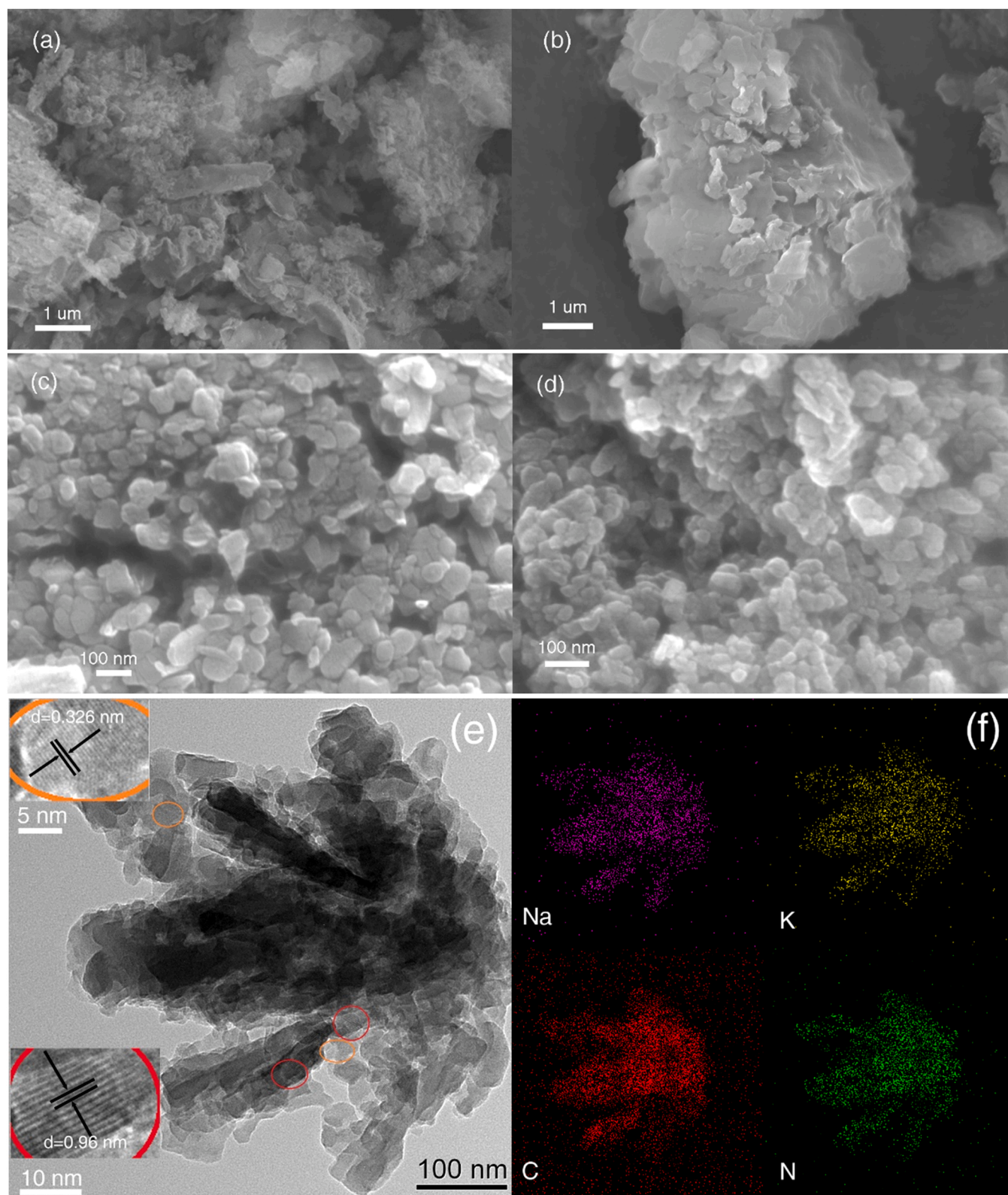


Fig. 2. X-ray photoelectron spectra of the samples DCN, DCN-NaK and DCN-NaK-90ABN: (a) N 1s and (b) C 1s; (c) Solid-state  $^{13}\text{C}$  NMR spectra of DCN-NaK and DCN-NaK-90ABN.

of DCN can be fitted into three peaks at 284.8, 286.4 and 288.3 eV, corresponding to the  $\text{sp}^2$ -hybridized carbon of  $\text{C}=\text{C}/\text{C}-\text{C}$ ,  $\text{C}-\text{NH}_x$  and  $\text{C}-(\text{N})_3$ , respectively. Compared with DCN, two obvious new peaks for DCN-NaK and DCN-NaK-90ABN appear at 295.7 and 293.0 eV, originating from the constituent N-K bond [39,40]. The same situation can also be observed from the Na 1s spectra (Fig. S2b, Supporting Information) [41]. The introduced K/Na ions are most likely as a charge compensator to balance the missing H of  $\text{NH}_3$  in the thermal polymerization of molten salt (Scheme S2, Supporting Information). Owing to the cyano groups ( $\text{C}\equiv\text{N}$ ) possess similar C1 s binding energies to  $\text{C}-\text{NH}_x$  [42,43], the signals at around 286.7 eV for DCN-NaK and DCN-NaK-90ABN are significantly enhanced in comparison with that of DCN, further verified the formation of  $\text{C}\equiv\text{N}$  groups in the eutectic NaCl-KCl salts [18]. The integral peak area ratio of  $\text{sp}^2$ -hybridized carbon in the C 1s spectra is significantly improved from 0.08 for DCN to 0.15 for DCN-NaK, which can be attributed to the formation of N-defects by the treatment of NaCl-KCl molten salt. The ratio for DCN-NaK-90ABN further raises to 0.19, which is derived from the grafted benzene ring by the incorporation of ABN (Scheme S2) [38]. In addition, because of the formational  $\text{C}\equiv\text{N}$  with strong electron-withdrawing effect in eutectic NaCl-KCl salt, the  $\text{C}-(\text{N})_3$  in the C 1s XPS spectra and all the peaks in the N 1s XPS spectra of DCN-NaK and DCN-NaK-90ABN exhibit a small shift

to lower binding energy compared with DCN [22,43]. Meanwhile, the similar negative shift for  $\text{C}-(\text{N})_3$  in the C 1s XPS spectrum and  $\text{sp}^2$   $\text{C}-\text{N}=\text{C}/\text{N}-(\text{C})_3$  in the N 1s XPS spectrum can be observed from DCN-NaK to DCN-NaK-90ABN, which can be attributed to the redistribution of electrons accompanying with the incorporation of ABN in the structure of DCN-NaK. The  $\text{C}-\text{N}=\text{C}$  and  $\text{N}-(\text{C})_3$  signals indicate the maintained on-plane repeating heptazine units for DCN-NaK-90ABN. For further investigating the framework structure of as-prepared samples, the solid-state  $^{13}\text{C}$  NMR spectra were adopted (Fig. 2c). The spectrum for DCN-NaK is very similar to that for DCN-NaK-90ABN. Two typical characteristic peaks at 162.8 and 156.2 ppm for DCN-NaK can be detected, corresponding to the carbon atoms of melem ( $\text{CN}_3$ , 1) and  $\text{CN}_2(\text{NH}_x)$  (2) in the heptazine units, respectively [44]. The chemical shifts of DCN-NaK-90ABN move slightly to high fields (Fig. 2c, inset), implying the improved electron delocalization [7]. The peaks at 168.0 and 111.0 ppm for DCN-NaK and DCN-NaK-xABN can be observed, which can be ascribed to the formational  $\text{C}\equiv\text{N}$  structure (4) and neighbor carbon atoms (3), respectively [45,46]. A new peak assigned to the incorporated aromatic carbon from ABN appears at 125.6 ppm [38]. Based on the above discussions, it can be inferred that the aromatic ring structure can be grafted into the CN framework by the incorporation of ABN. The use of eutectic NaCl-KCl salt leads to the nitrogen defects and





**Fig. 3.** SEM images of (a) DCN, (b) DCN-90ABN, (c) DCN-NaK and (d) DCN-NaK-90ABN; (e) HRTEM images and (f) the corresponding elemental mapping results of DCN-NaK-90ABN.

-C≡N. The K/Na ions are introduced by balancing the charge of C-N<sup>+</sup>-C. In addition, the basic heptazine ring units are well maintained. The reasonable structure for DCN-NaK-xABN is proposed in [Scheme S2](#).

The morphology and microstructure of as-prepared samples were investigated by SEM and TEM ([Fig. 3](#)). DCN and DCN-90ABN exhibit an

irregular stacked lamellar structure ([Figs. 3a and 3b](#)). With the treatment of NaCl-KCl eutectic salt, the particles size of DCN-NaK shows an obvious reduction ( $\sim 100$  nm) and high uniformity ([Fig. 3c](#)). Further reduced particle size ( $\sim 50$  nm, [Fig. 3d](#)) can be observed for DCN-NaK-90ABN, which can attribute to the polymerized disruption with the

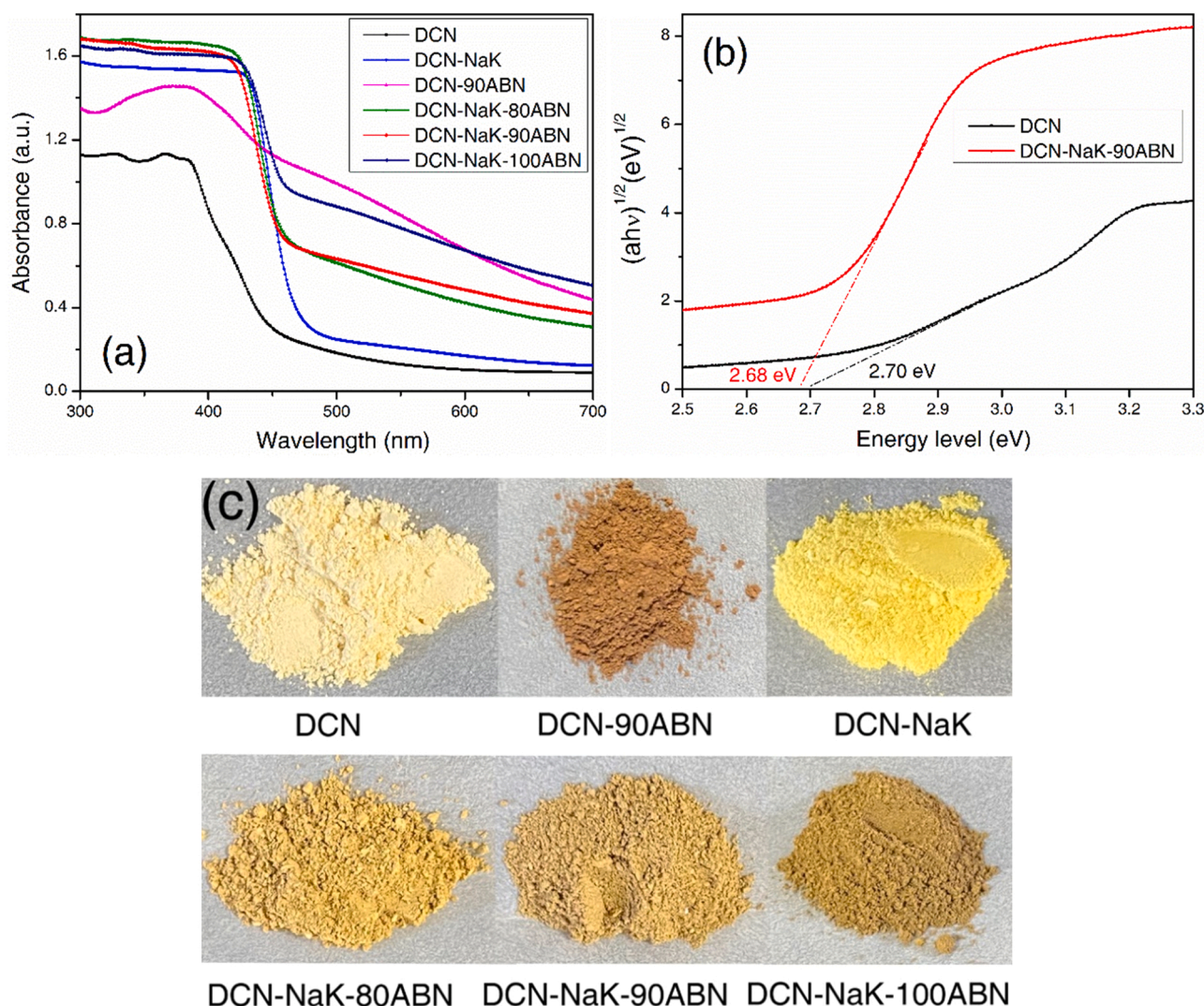


**Fig. 4.** (a) UV–vis light absorption spectra of DCN, DCN-NaK, DCN-90ABN and DCN-NaK-xABN and (c) these corresponding color; (b) band gap energy of DCN and DCN-NaK-90ABN.

introduction of aromatic ring (Scheme S2). The small nanosheets with even distribution are recorded by TEM (Fig. 3e). Furthermore, two different lattice fringes 0.960 nm and 0.326 nm can be observed (Fig. 3e, inset), which are in good accordance with the (100) and (002) plane of DCN-NaK-90ABN, respectively (Fig. 1a). The EDX mapping reveals the uniform distribution of C, N, Na and K in DCN-NaK-90ABN, consistent with the XPS results (Fig. S2a, Supporting Information). Moreover, a classical type IV isotherms with the  $H_3$  hysteresis loop for the as-prepared catalysts (Figs. S3a–3f, Supporting Information) are displayed by the nitrogen adsorption and desorption isotherms measurements, indicating the existence of mesopores derived from nanosheet stacking. The BET specific surface areas ( $S_{\text{BET}}$ ) of DCN, DCN-90ABN, DCN-NaK and DCN-NaK-xABN are shown in Table 1. DCN-NaK-80ABN ( $37.2 \text{ m}^2/\text{g}$ ) and DCN-NaK-90ABN ( $34.1 \text{ m}^2/\text{g}$ ) show larger  $S_{\text{BET}}$  than DCN ( $23.1 \text{ m}^2/\text{g}$ ), because of the decreased particle size (Fig. 3d). Although the specific surface areas play an important role in photocatalytic activity, the slight variation in  $S_{\text{BET}}$  for DCN-NaK-xABN demonstrates the significantly magnified photocatalytic activity (Fig. 8 and Fig. 9) due to the unique structural and optical properties. In addition,  $S_{\text{BET}}$  of DCN-NaK-100ABN presents a slight reduction because of the excessive loading of ABN.

### 3.2. Optical property and band structure

UV–vis diffuse reflectance spectra of DCN, DCN-NaK, DCN-90ABN and DCN-NaK-xABN are shown in Fig. 4a. All of DCN-NaK and DCN-NaK-xABN show notable enhancement of visible light absorption in the range of 300–460 nm compared to DCN, which can attribute to the introduction of nitrogen defects and cyano groups. More importantly, with the increased loading of ABN, the optical absorption for DCN-NaK-xABN is gradually increased between 460 nm 700 nm, originating from the grafted benzene ring as well as the improved delocalization. The enhanced optical absorption of the samples indicates stabilized electron and hole in the excited state [47], suggesting the photochemistry can potentially be utilized even under the wavelength longer than 500 nm. The color of sample is gradually deepened from pale yellow for DCN to bright yellow for DCN-NaK and brownish yellow for DCN-NaK-90ABN (Fig. 4c). The bandgaps of DCN and DCN-NaK-90ABN were further analyzed by the Kubelka-Munk plot (Fig. 4b), which are corresponding to 2.70 and 2.68 eV, respectively.

For investigating the band structure, the Mott-Schottky and valence band X-ray photoelectron spectroscopy (VB XPS) were adopted. Both the Mott-Schottky plots (Figs. 5a and 5b) for DCN and DCN-NaK-90ABN present positive slopes at different frequencies, demonstrating the typical n-type semiconducting nature. The Fermi level is determined to



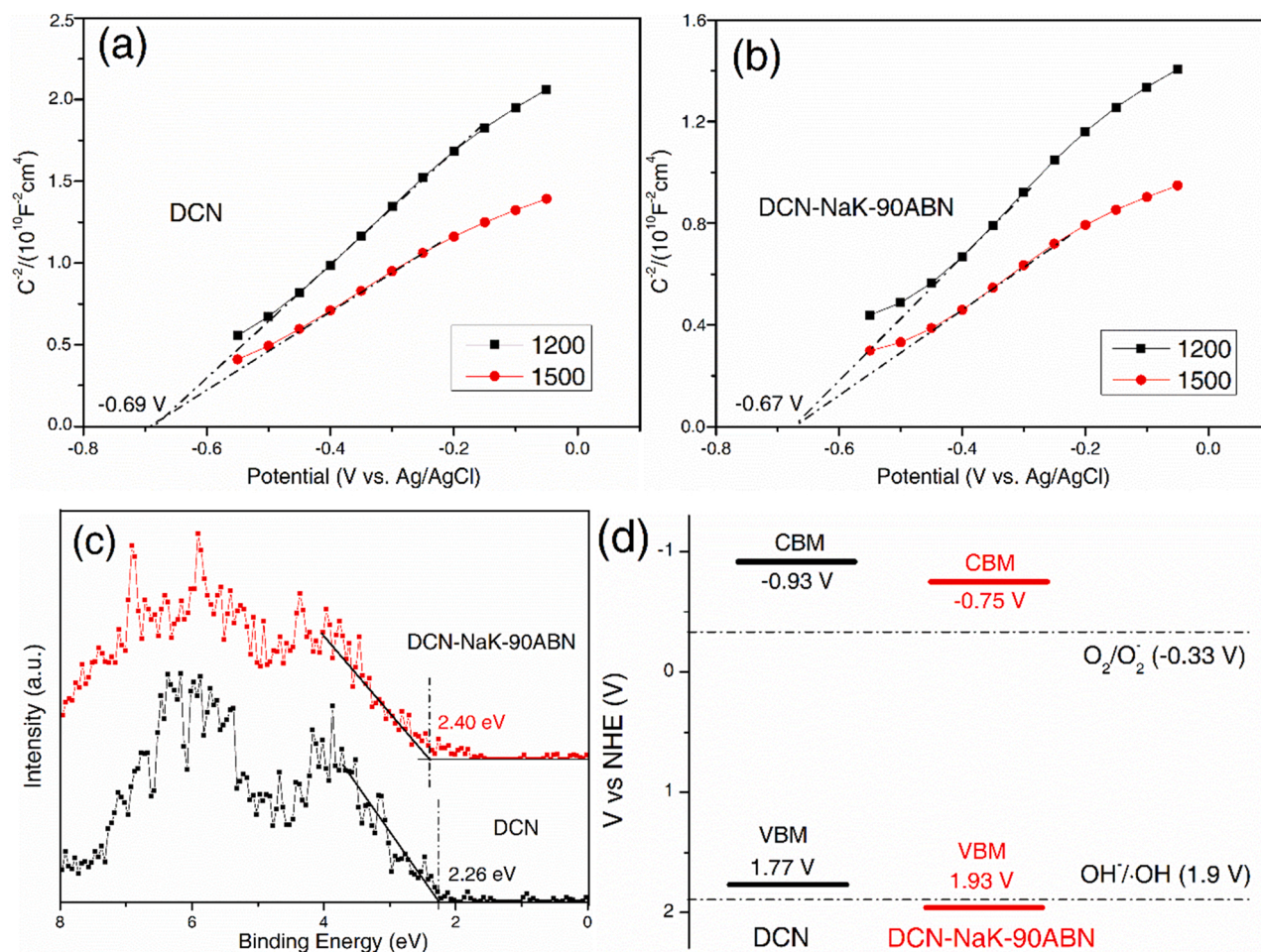


Fig. 5. Mott-Schottky plots of (a) DCN and (b) DCN-NaK-90ABN at different frequencies; (c) VB-XPS and (d) band structure of DCN and DCN-NaK-90ABN.

be  $-0.69$  V for DCN and  $-0.67$  V for DCN-NaK-90ABN (vs. Ag/AgCl), corresponding to  $-0.49$  and  $-0.47$  V (vs. NHE), respectively [48,49]. The VB-XPS spectra (Fig. 5c) display that the binding energies for DCN and DCN-NaK-90ABN are 2.26 and 2.40 eV, respectively. Furthermore, taking into account the binding energies in the VB XPS spectra and the difference between valence band maximum (VBM) and Fermi level [50, 51], the VBM can be calculated to be 1.77 V for DCN and 1.93 V for DCN-NaK-90ABN (vs. NHE), respectively. Combined with the bandgaps in Fig. 4b, the conduction band minimum (CBM) is  $-0.93$  and  $-0.75$  V for DCN and DCN-NaK-90ABN (vs. NHE), respectively. The corresponding band structure of DCN and DCN-NaK-90ABN are shown in Fig. 5d. The VBM of DCN-NaK-90ABN exhibits a positive shift compared to DCN, indicating the better potential in the oxidation ability. Compared with the more negative VBM position for DCN (1.77 V), the VBM for DCN-NaK-90ABN (1.93 V) is more positive than the potential of  $\text{OH}^-/\text{OH}$  (1.9 V vs NHE), suggesting DCN-NaK-90ABN can produce the active species  $\cdot\text{OH}$  under illumination. The phenomenon is consistent with the results in Fig. 8b and Fig. S4. The improved oxidation capacity and the generated active species ( $\cdot\text{OH}$ ) for DCN-NaK-90ABN are attributed to the excellent performance in the photodegradation of BPA (Fig. 8). In addition, although DCN-NaK-90ABN displayed a positive shift in the CBM, the potential in DCN-NaK-90ABN is still negative enough to promote the proton reduction from water ( $\text{H}_2$  generation).

### 3.3. Theoretical simulation

Density functional theory (DFT) calculations were adopted to investigate the electronic structures of DCN and DCN-NaK-xABN

(Fig. 6). The density of states (DOS, Fig. 6a) for the C and N atomic orbitals in the optimized structure of DCN-NaK-xABN exhibit a high coincidence degree in the peak position, indicating the stable existence for the proposed structure in Scheme S2. The bandgap of DCN-NaK-xABN is narrower than that of DCN in good agreement with the experiment results in Fig. 4b, verifying the enhanced delocalization for DCN-NaK-xABN. Furthermore, the lowest unoccupied molecular orbital (LUMO) is contributed by the C 2p and N 2p orbitals, while the highest occupied molecular orbital (HOMO) is mainly located on the N 2p orbitals for DCN in Fig. 6b. Owing to the overlapped distribution of N 2p orbitals in pristine PCN, the photogenerated carrier will have a high recombination rate and inhibit the photocatalytic active [52]. With the treatment of NaCl-KCl molten salt and the incorporation of ABN, the obtained frontier orbitals of DCN-NaK-xABN demonstrates notable change in their wave function distributions (Fig. 6c). The contrasting distribution of HOMO and LUMO in the CN network indicates the improved spatial separation of photogenerated carriers, which will be conducive to the transfer of electrons in plane and the improvement of photocatalytic performance.

### 3.4. The transfer behavior of electrons

The charge carrier behavior could be detected by the photoluminescence (PL) spectra (Fig. 7a). With the use of NaCl-KCl molten salt or ABN, the PL intensities are obviously decreased with respect to the DCN, because of the formational defect-containing (e.g.,  $-\text{C}\equiv\text{N}$  and nitrogen defect) in DCN-NaK and the enhanced delocalization in DCN-NaK-90ABN [22,26]. The PL intensities for DCN-NaK-xABN are further



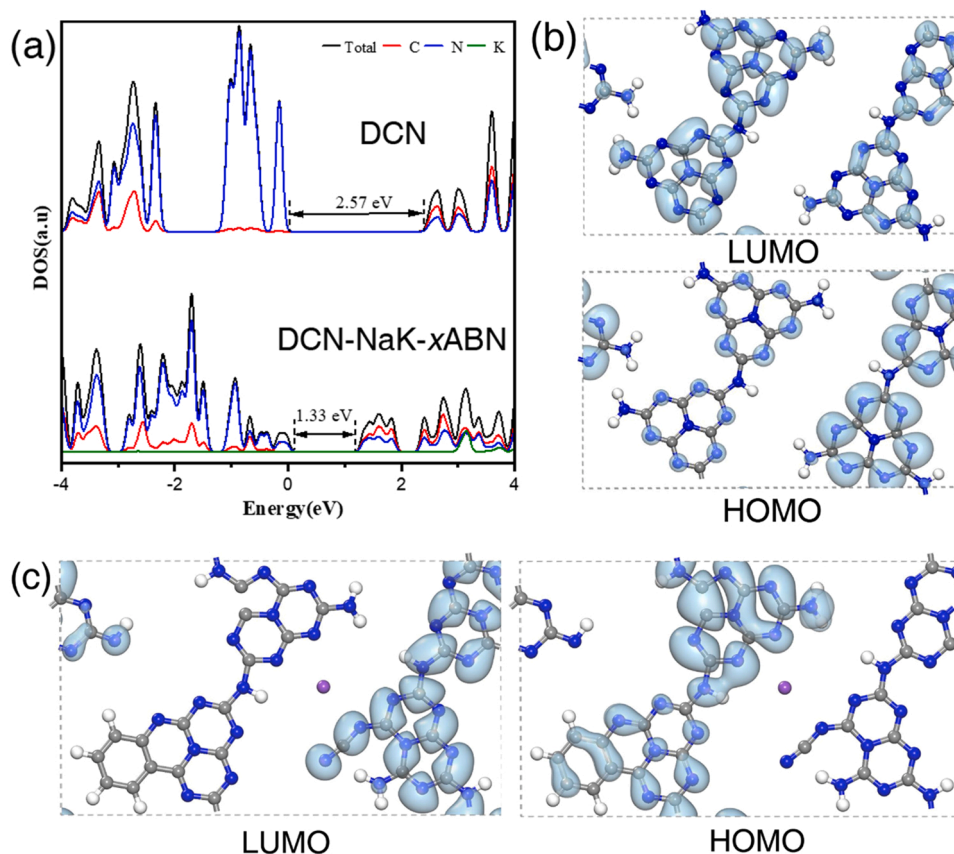


Fig. 6. (a) DFT calculated DOS, HOMO and LUMO distributions of (b) DCN and (c) DCN-NaK-xABN.

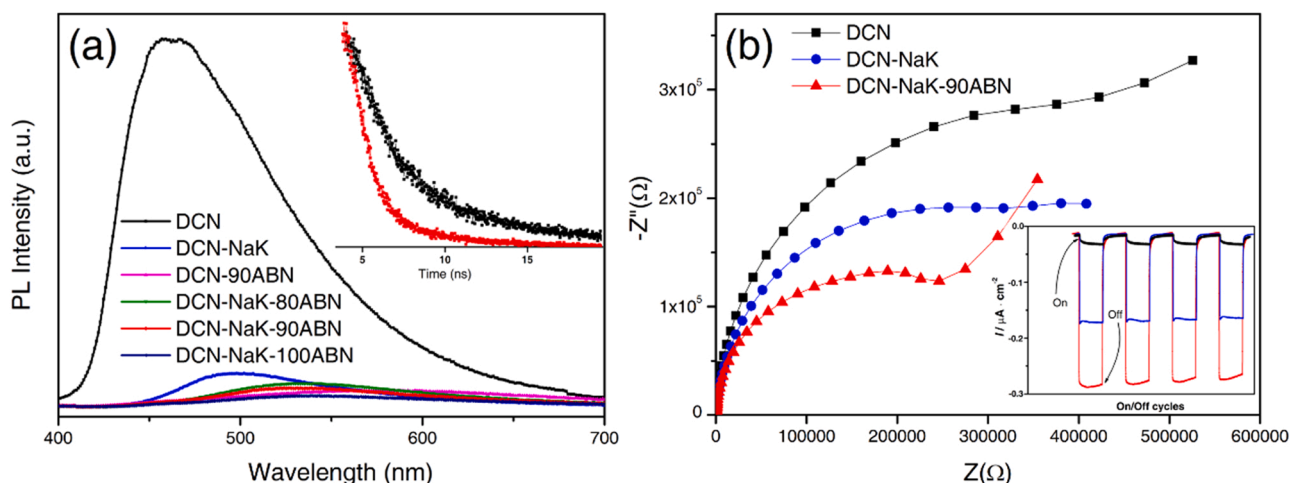
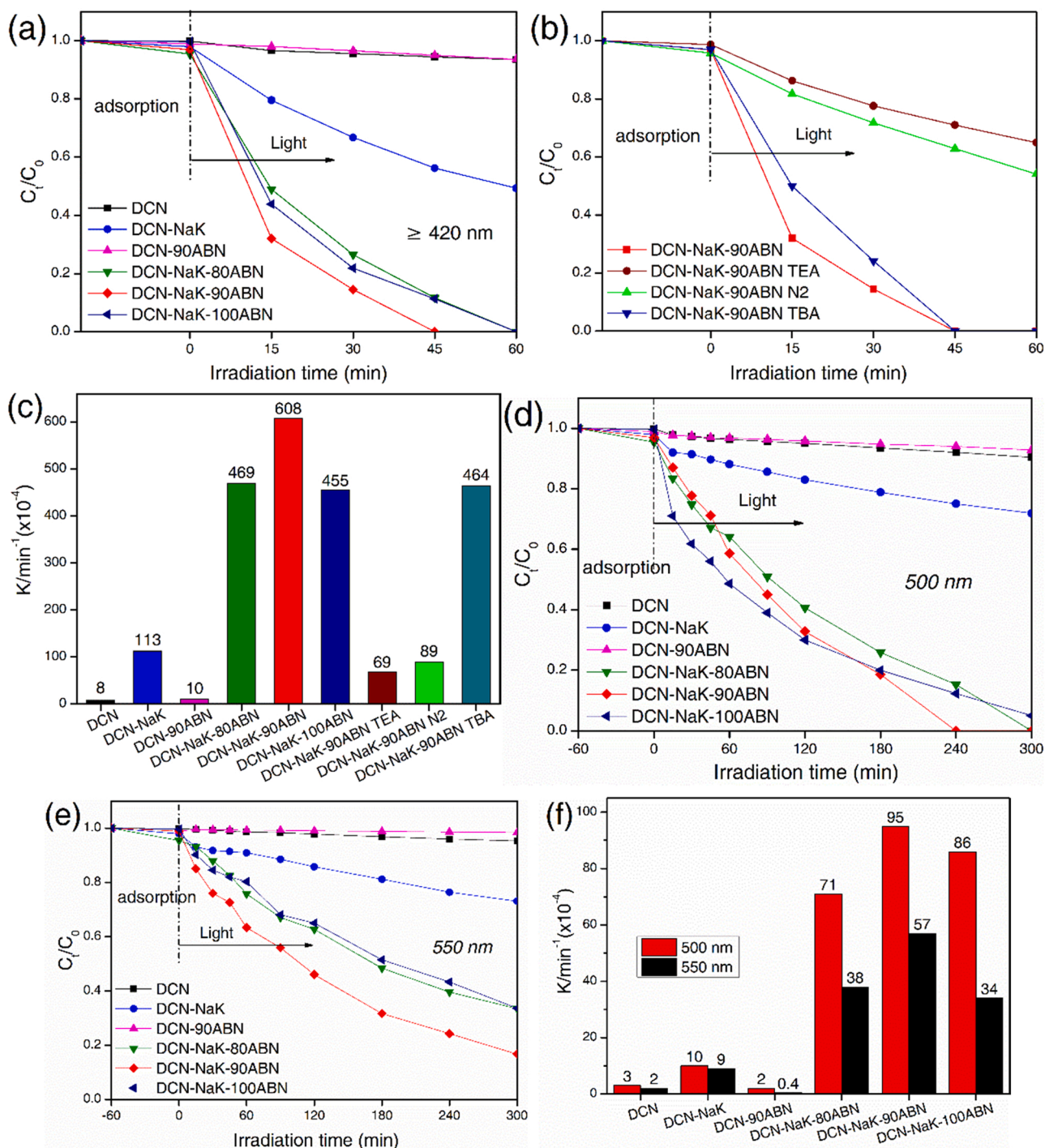


Fig. 7. (a) PL spectra of DCN, DCN-90ABN, DCN-NaK and DCN-NaK-90ABN, inset: time-resolved fluorescence kinetics of DCN and DCN-NaK-90ABN monitored at 460 nm under 340 nm excitation; (b) photocurrent and EIS Nyquist plots in the dark of DCN, DCN-NaK and DCN-NaK-90ABN.

reduced, indicating the effective defect-containing and delocalization. The significant decay in peak intensity demonstrates the reduced charge carrier recombination. In addition, a progressive redshift can be observed from 462 nm for DCN to 498 nm for DCN-NaK and 533 nm for DCN-NaK-90ABN, respectively, highlighting the improved stabilization for the photogenerated electrons and holes [23]. Time-resolved fluorescence spectra were adopted to further explore the photoexcited charge carriers (Fig. 7a, inset). The mean radiative lifetimes ( $\tau_r$ ) of DCN and DCN-NaK-90ABN were 5.91 and 2.80 ns, respectively (Table S1, Supporting Information). The notably decreased singlet exciton lifetime

for DCN-NaK-90ABN in comparison with that of DCN implies the improved exciton dissociation. Probably, the enhanced electron delocalization and formational defect in DCN-NaK-90ABN promote the singlet excitons to dissociate, and then inhibit the recombination of charge carrier. The charge-transfer properties of DCN, DCN-NaK and DCN-NaK-90ABN were further investigated by the Nyquist plots of Electrochemical impedance spectroscopy (EIS) and photocurrent (Fig. 7b). The reduced EIS radius from DCN to DCN-NaK and DCN-NaK-90ABN can be observed, implying that the electron transfer resistance is decreased gradually by using the NaCl-KCl molten salt and



**Fig. 8.** (a, b) Photocatalytic degradation profiles and (c) rate constant  $k$  of BPA under visible light irradiation; Photocatalytic degradation profiles of BPA at (d) 500 nm and (e) 550 nm illumination and (f) corresponding to the rate constant  $k$ .

ABN. The photocharge densities of DCN-NaK-90ABN and DCN-NaK are eight and five times higher than that of DCN, respectively, further demonstrating the significant improvement of charge transfer [53,54]. Based on the above results, the photoinduced excitons of DCN-NaK-90ABN can be effectively separated and transferred, which can be beneficial to the enhancement of photocatalytic activity.

### 3.5. Photocatalytic performance

#### 3.5.1. Photodegradation of bisphenol A (BPA) and mechanism

The photodegradation of BPA is investigated to explore the

photocatalytic activity (Fig. 8). Weak adsorption for BPA ( $< 4.5\%$ ) can be observed among all the samples, indicating the adsorption does not play the critical role in the photocatalysis. The photodegradation efficiency of BPA under visible light irradiation for 45 min can reach to 88.3% for DCN-NaK-80ABN, 100% for DCN-NaK-90ABN and 88.7% for DCN-NaK-100ABN, respectively (Fig. 8a), which are much higher than those for DCN (only 5.6%), DCN-NaK (43.8%) and for DCN-90ABN (5.1%), demonstrating that the formational defect-containing and enhanced delocalization in DCN-NaK-xABN are effective to improve the photocatalytic activity. Furthermore, to explore the mechanism in the photocatalytic process, radical scavengers were adopted [55,56]. As

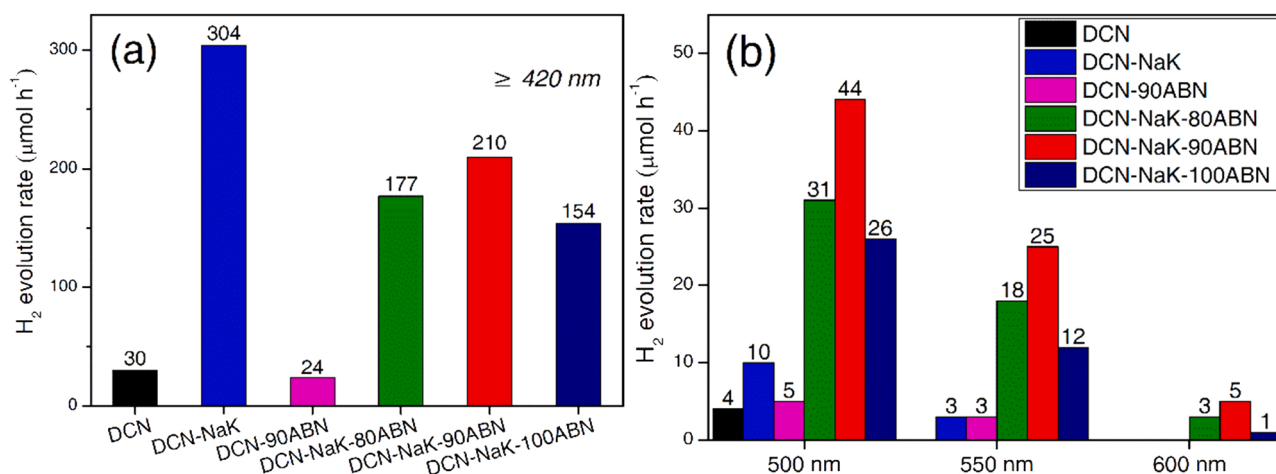


Fig. 9. Hydrogen evolution rate of DCN, DCN-NaK, DCN-90ABN and DCN-NaK-xABN under (a) visible light ( $\lambda \geq 420$  nm), (b) 500, 550 and 600 nm irradiation.

depicted in Fig. 8b, the photodegradation efficiency of DCN-NaK-90ABN for BPA is notably decreased as TEA or N<sub>2</sub> gas flow is introduced into the system. In detail, the removal efficiency of BPA is only 22.4% and 28.3% with TEA and N<sub>2</sub> gas flow within 30 min, respectively, whereas the degradation rate can reach to 85.5% in 30 min without them in the system. The results suggest that positive holes ( $h^+$ ) and  $\cdot O_2$  are main active species in the photocatalytic process. Besides, the removal rate is partially reduced when TBA is added (75.9% for 30 min), suggesting  $\cdot OH$  can also act as the active species in the system. The generated active free radicals for DCN-NaK-90ABN and DCN could be further monitored by the ESR (Fig. 4S, Supporting Information) [48,49]. The photogenerated carrier (electrons and holes) and oxygen-containing groups ( $\cdot OH$  and  $\cdot O_2$ ) can be detected in DCN-NaK-90ABN under visible light irradiation, consistent with the above results in Fig. 8b. Furthermore, the ESR signal of DCN-NaK-90ABN is significantly weakened than that of DCN under the same illumination conditions (Fig. S4b), indicating that more photogenerated holes are produced in DCN-NaK-90ABN. The results can ascribe to the specific chemical construction of DCN-NaK-90ABN accompanying with the better potential in the oxidation ability according to the band structure (Fig. 5d). The peak intensity of DCN-NaK-90ABN is also higher than that of DCN in Fig. S4d, indicating DCN-NaK-90ABN can generate more  $\cdot O_2$ . The more active species for DCN-NaK-90ABN can be beneficial to the photocatalytic activity.

The kinetic data for the photodegradation can be well fitted according to the pseudo-first-order correlation (Fig. S5a and S5b, Supporting Information). The related reaction rate constants ( $k$ ) are shown in Fig. 8c. The  $k$  value for DCN-NaK-90ABN is  $608 \times 10^{-4} \text{ min}^{-1}$ , which is about 76.0, 5.4 and 60.8 times higher than those of DCN ( $8 \times 10^{-4} \text{ min}^{-1}$ ), DCN-NaK ( $113 \times 10^{-4} \text{ min}^{-1}$ ) and DCN-90ABN ( $10 \times 10^{-4} \text{ min}^{-1}$ ), respectively, implying that the incorporation of ABN and the treatment of NaCl-KCl eutectic salt are vital to improve the performance. The rate constant fluctuates with the content of ABN in DCN-NaK-xABN ( $469 \times 10^{-4} \text{ min}^{-1}$  for DCN-NaK-80ABN and  $455 \times 10^{-4} \text{ min}^{-1}$  for DCN-NaK-100ABN), indicating the effective incorporation depends on the amount of ABN. With the introduction of TEA, TBA or N<sub>2</sub> gas flow, the  $k$  value is reduced to  $49 \times 10^{-4} \text{ min}^{-1}$ ,  $89 \times 10^{-4} \text{ min}^{-1}$  and  $464 \times 10^{-4} \text{ min}^{-1}$ , respectively. The results reveal the effect of different active radicals ( $h^+ > \cdot O_2 > \cdot OH$ ) in the photodegradation process. Furthermore, considering the enhanced delocalization accompanying with the significant improvement of optical absorption in the range of long wavelength by the incorporation of ABN, the photodegradation for BPA was carried out at 500 nm and 550 nm, respectively (Fig. 8d and Fig. 8e). After fitting the suitable pseudo-first-order correlation (Fig. S5c and S5d, Supporting Information), the  $k$  value was shown in Fig. 8f. Compared with the weak rate constant of DCN-NaK at the irradiation of 500 nm and 550 nm, the  $k$  values of DCN-NaK-xABN still maintain high,

indicating the incorporation of ABN as well as the enhanced delocalization promotes the photodegradation performance at the long wavelength range. In addition, the stability of DCN-NaK-90ABN before and after two cycles test of photodegradation was explored by XRD measurements (Fig. S5e, Supporting Information). The XRD patterns have no notably change, showing its high phase stability.

To clarify the degradation pathway of DCN-NaK-90ABN for BPA, LC-MS was used to examine the intermediates and products. Ten molecules can be detected from the mass spectra (Fig. S6, Supporting Information). The  $-m/z = 227$  is the BPA molecular ion. At the beginning of the photodegradation process, BPA would be decomposed into 2 kinds of intermediates products, indicating the loss of a methyl group ( $-m/z = 213$ ) and the formation of hydroxylated derivatives ( $-m/z = 243$ ) [57]. Subsequently, continuous ring cleavage can open one of the aromatic rings to generate several intermediates ( $-m/z = 232, 133, 107, 151$ ) with one aromatic ring by the continuous oxidation [58]. Finally, the aromatic rings are opened ( $-m/z = 101$  and 117). The total organic carbon (TOC) removal efficiency of DCN-NaK-90ABN in the system can reach up to 75% within 45 min. We believe that these small molecules may be decomposed into CO<sub>2</sub> and H<sub>2</sub>O eventually after sufficient reaction time. The possible reaction route has been proposed in the Fig. S7.

### 3.5.2. Photocatalytic hydrogen evolution (PHE)

The PHE was also performed to confirm the improved photocatalytic activity (Fig. 9). As shown in Fig. 9a, all of DCN-NaK ( $304 \mu\text{mol h}^{-1}$ ), DCN-NaK-80ABN ( $177 \mu\text{mol h}^{-1}$ ), DCN-NaK-90ABN ( $210 \mu\text{mol h}^{-1}$ ) and DCN-NaK-100ABN ( $154 \mu\text{mol h}^{-1}$ ) exhibit significant improvement in hydrogen evolution rate (HER) compared with DCN ( $30 \mu\text{mol h}^{-1}$ ) and DCN-90ABN ( $24 \mu\text{mol h}^{-1}$ ). Interestingly, the HER of DCN-NaK-xABN is dramatically enhanced under the irradiation of above 500 nm due to the promoted optical absorption (Fig. 9b). Especially, the HER performance of DCN-NaK-90ABN can reach to  $44 \mu\text{mol h}^{-1}$  (AQE = 8.15%) at 500 nm and  $25 \mu\text{mol h}^{-1}$  (AQE = 4.01%) at 550 nm, while those of DCN are  $4 \mu\text{mol h}^{-1}$  (AQE = 0.74%) at 500 nm and  $0 \mu\text{mol h}^{-1}$  at 550 nm. Even the HER of DCN-NaK is only  $10 \mu\text{mol h}^{-1}$  (AQE = 1.85%) at 500 nm and  $3 \mu\text{mol h}^{-1}$  (AQE = 0.48%) at 550 nm. The PHE efficiency of DCN-NaK-90ABN is much higher than those of most previously reported PCN-based photocatalysts (Table S2, Supporting Information). This phenomenon reveals that abundant photons can be harvested by DCN-NaK-xABN in a long wavelength range to drive the photoreaction due to the incorporation of ABN into the CN framework. In addition, five cycles tests are performed in 20 h (Fig. S8, Supporting Information), the PHE performance is stable without obvious deactivation, which is vital for catalyst in practical application.



## 4. Conclusion

The enhanced electron delocalization and formational defect-containing ( $\text{C}\equiv\text{N}$  and nitrogen defect) in PCN-based photocatalyst are successfully achieved by the assistance of NaCl-KCl molten salts and the incorporation of ABN. The obtained composites, DCN-NaK-xABN, can harvest much more photons under visible light irradiation and suppress the recombination of photogenerated carriers, resulting in the significant improvement in PHE and photodegradation of BPA. Especially, the composites show high photocatalytic activity in the green light region. The work provides a new avenue to optimize the physicochemical properties of polymeric light collectors for improved solar energy harvesting.

## CRediT authorship contribution statement

**Chengqun Xu:** Conceptualization, Project administration, Funding acquisition, Writing – original draft. **Haiyang Liu:** Data curation, Methodology, Writing – original draft. **Dongyu Wang:** Data curation, Methodology, Writing – original draft. **Dezhi Li:** Investigation, Validation. **Xiaolu Liu:** Investigation, Validation. **Jingyao Huang:** Validation. **Shengquan Wu:** Validation. **Donghua Fan:** Methodology and Formal analysis. **Ying Zhang:** Software. **Hongguang Liu:** Software. **Hui Pan:** Writing – review & editing, Supervision.

## Declaration of Competing Interest

The authors declare that they have no known competing financial interests or personal relationships that could have appeared to influence the work reported in this paper.

## Data Availability

Data will be made available on request.

## Acknowledgements

Chengqun Xu acknowledges the Guangdong Basic and Applied Basic Research Foundation (2019A1515110154), Natural Science Foundation of Guangdong Province (2018A030313460) and Key Laboratory of Optoelectronic Materials and Applications in Guangdong Higher Education (2017KSYS011) for the financial support. Hui Pan thanks the supports from the Science and Technology Development Fund (FDCT) from Macau SAR (0081/2019/AMJ, 0154/2019/A3, 006/2022/ALC, and 0111/2022/A2), Multi-Year Research Grants (MYRG2022–00026-IAPME) from Research & Development Office at University of Macau, and Shenzhen-Hong Kong-Macao Science and Technology Research Programme (Type C) (SGDX20210823103803017) from Shenzhen.

## Appendix A. Supporting information

Supplementary data associated with this article can be found in the online version at [doi:10.1016/j.apcatb.2023.122835](https://doi.org/10.1016/j.apcatb.2023.122835).

## References

- [1] S. Cao, J. Low, J. Yu, M. Jaroniec, *Adv. Mater.* 27 (2015) 2150–2176.
- [2] J. Zhang, Y. Chen, X. Wang, *Energ. Environ. Sci.* 8 (2015) 3092–3108.
- [3] J. Zhao, M. Ji, H. Chen, Y. Weng, J. Zhong, Y. Li, S. Wang, Z. Chen, J. Xia, H. Li, *Appl. Catal. B: Environ.* 307 (2022), 121162.
- [4] H. Pan, *Renew. Sust. Energ. Rev.* 57 (2016) 584–601.
- [5] M. Shao, Y. Shao, S. Ding, J. Wang, J. Xu, Y. Qu, X. Zhong, X. Chen, W.F. Ip, N. Wang, *Appl. Catal. B: Environ.* 237 (2018) 295–301.
- [6] J. Zhang, J. Sun, K. Maeda, K. Domen, P. Liu, M. Antonietti, X. Fu, X. Wang, *Energ. Environ. Sci.* 4 (2011) 675–678.
- [7] Y. Chen, F. Su, H. Xie, R. Wang, C. Ding, J. Huang, Y. Xu, L. Ye, *Chem. Eur. J.* 404 (2021), 126498.
- [8] W. Cui, L. Chen, J. Sheng, J. Li, H. Wang, Y. Zhou, Y. Sun, F. Dong, *Appl. Catal. B: Environ.* 262 (2020), 118251.
- [9] H.J. Kong, D.H. Won, J. Kim, S.I. Woo, *Chem. Mater.* 28 (2016) 1318–1324.
- [10] C. Liu, H. Huang, L. Ye, S. Yu, N. Tian, X. Du, T. Zhang, Y. Zhang, *Nano Energy* 41 (2017) 738–748.
- [11] M. Shao, Y. Shao, J. Chai, Y. Qu, M. Yang, Z. Wang, M. Yang, W.F. Ip, C.T. Kwok, X. Shi, J. Mater. Chem. A 5 (2017) 16748–16756.
- [12] M.K. Bhunia, K. Yamauchi, K. Takanabe, *Angew. Chem. Int. Ed.* 126 (2014) 11181–11185.
- [13] L. Huang, Z. Hu, H. Jin, J. Wu, K. Liu, Z. Xu, J. Wan, H. Zhou, J. Duan, B. Hu, *Adv. Funct. Mater.* 30 (2020), 1908486.
- [14] X. Liu, N. Fechner, M. Antonietti, *Chem. Soc. Rev.* 42 (2013) 8237–8265.
- [15] M.J. Bojdys, J.O. Müller, M. Antonietti, A. Thomas, *Chem. Eur. J.* 14 (2008) 8177–8182.
- [16] G. Zhang, G. Li, Z. Lan, L. Lin, A. Savateev, T. Heil, S. Zafeirotas, X. Wang, M. Antonietti, *Angew. Chem. Int. Ed.* 129 (2017) 13630–13634.
- [17] L. Lin, W. Ren, C. Wang, A. Asiri, J. Zhang, X. Wang, *Appl. Catal. B: Environ.* 231 (2018) 234–241.
- [18] J. Liu, W. Fang, Z. Wei, Z. Qin, Z. Jiang, W. Shangguan, *Appl. Catal. B: Environ.* 238 (2018) 465–470.
- [19] G. Algara Siller, N. Severin, S.Y. Chong, T. Björkman, R.G. Palgrave, A. Laybourn, M. Antonietti, Y.Z. Khimyak, A.V. Krasheninnikov, J.P. Rabe, *Angew. Chem. Int. Ed.* 53 (2014) 7450–7455.
- [20] L. Lin, C. Wang, W. Ren, H. Ou, Y. Zhang, X. Wang, *Chem. Sci.* 8 (2017) 5506–5511.
- [21] L. Lin, H. Ou, Y. Zhang, X. Wang, *ACS Catal.* 6 (2016) 3921–3931.
- [22] G. Zhang, G. Li, T. Heil, S. Zafeirotas, F. Lai, A. Savateev, M. Antonietti, X. Wang, *Angew. Chem. Int. Ed.* 58 (2019) 3433–3437.
- [23] G. Zhang, L. Lin, G. Li, Y. Zhang, A. Savateev, S. Zafeirotas, X. Wang, M. Antonietti, *Angew. Chem. Int. Ed.* 130 (2018) 9516–9520.
- [24] M. Zhang, X. Wang, *Energ. Environ. Sci.* 7 (2014) 1902–1906.
- [25] J. Liu, Y. Yu, R. Qi, C. Cao, X. Liu, Y. Zheng, W. Song, *Appl. Catal. B: Environ.* 244 (2019) 459–464.
- [26] C. Xu, X. Liu, D. Li, Z. Chen, J. Yang, J. Huang, H. Pan, *ACS Appl. Mater. Inter.* 13 (2021) 20114–20124.
- [27] C. Xu, W. Zhang, K. Deguchi, S. Ohki, T. Shimizu, R. Ma, T. Sasaki, *J. Mater. Chem. A* 8 (2020) 13299–13310.
- [28] C. Xu, X. Liu, H. Liu, D. Li, Y. Yang, S. Lin, D. Fan, H. Pan, *J. Mater. Chem. A* 10 (2022) 21031–21043.
- [29] J.P. Perdew, K. Burke, M. Ernzerhof, *Phys. Rev. Lett.* 77 (1996) 3865.
- [30] M. Segall, P.J. Lindan, M. Probert, C.J. Pickard, P.J. Hasnip, S. Clark, M. Payne, *J. Phys. Condens. Mat.* 14 (2002) 2717.
- [31] C. Xu, K. Li, W. Zhang, *J. Colloid Interf. Sci.* 495 (2017) 27–36.
- [32] G. Zhang, G. Li, Z. Lan, L. Lin, A. Savateev, T. Heil, S. Zafeirotas, X. Wang, M. Antonietti, *Angew. Chem. Int. Ed.* 129 (2017) 13630–13634.
- [33] Y. Guo, J. Li, Y. Yuan, L. Li, M. Zhang, C. Zhou, Z. Lin, *Angew. Chem. Int. Ed.* 128 (2016) 14913–14917.
- [34] C. Xu, W. Zhang, *Mol. Catal.* 453 (2018) 85–92.
- [35] H. Gao, S. Yan, J. Wang, Y.A. Huang, P. Wang, Z. Li, Z. Zou, *Phys. Chem. Chem. Phys.* 15 (2013) 18077–18084.
- [36] V.N. Khabashesku, J.L. Zimmerman, J.L. Margrave, *Chem. Mater.* 12 (2000) 3264–3270.
- [37] X. Li, W. Bi, L. Zhang, S. Tao, W. Chu, Q. Zhang, Y. Luo, C. Wu, Y. Xie, *Adv. Mater.* 28 (2016) 2427–2431.
- [38] J. Zhang, G. Zhang, X. Chen, S. Lin, L. Möhlmann, G. Dolega, G. Lipner, M. Antonietti, S. Blechert, X. Wang, *Angew. Chem. Int. Ed.* 51 (2012) 3183–3187.
- [39] M. Zhang, X. Bai, D. Liu, J. Wang, Y. Zhu, *Appl. Catal. B: Environ.* 164 (2015) 77–81.
- [40] Y. Li, S. Ouyang, H. Xu, X. Wang, Y. Bi, Y. Zhang, J. Ye, *J. Am. Chem. Soc.* 138 (2016) 13289–13297.
- [41] Y. Zhang, S. Zong, C. Cheng, J. Shi, X. Guan, Y. Lu, L. Guo, *Int. J. Hydrog. Energ.* 43 (2018) 13953–13961.
- [42] D. Zhang, Y. Guo, Z. Zhao, *Appl. Catal. B: Environ.* 226 (2018) 1–9.
- [43] H. Yu, R. Shi, Y. Zhao, T. Bian, Y. Zhao, C. Zhou, G.I. Waterhouse, L. Wu, C. Tung, T. Zhang, *Adv. Mater.* 29 (2017), 1605148.
- [44] J.R. Holst, E.G. Gillan, *J. Am. Chem. Soc.* 130 (2008) 7373–7379.
- [45] J. Yuan, X. Liu, Y. Tang, Y. Zeng, L. Wang, S. Zhang, T. Cai, Y. Liu, S. Luo, Y. Pei, *Appl. Catal. B: Environ.* 237 (2018) 24–31.
- [46] V.W. Lau, I. Moudrakovski, T. Botari, S. Weinberger, M.B. Mesch, V. Duppel, J. Senker, V. Blum, B.V. Lotsch, *Nat. Commun.* 7 (2016) 1–10.
- [47] G. Zhang, Z. Lan, X. Wang, *Angew. Chem. Int. Ed.* 55 (2016) 15712–15727.
- [48] C. Xu, D. Li, X. Liu, R. Ma, N. Sakai, Y. Yang, S. Lin, J. Yang, H. Pan, J. Huang, *Chem. Eng. J.* 430 (2022), 132861.
- [49] C. Xu, D. Li, H. Liu, D. Wang, X. Liu, S. Lin, Y. Yang, D. Fan, H. Pan, *J. Environ. Chem. Eng.* (2022), 109191.
- [50] P. Xia, S. Cao, B. Zhu, M. Liu, M. Shi, J. Yu, Y. Zhang, *Angew. Chem. Int. Ed.* 59 (2020) 5218–5225.
- [51] F. Xu, K. Meng, B. Cheng, S. Wang, J. Xu, J. Yu, *Nat. Commun.* 11 (2020) 1–9.
- [52] X. Fan, L. Zhang, R. Cheng, M. Wang, M. Li, Y. Zhou, J. Shi, *A.C.S. Catal.* 5 (2015) 5008–5015.
- [53] R. Tong, K.W. Ng, X. Wang, S. Wang, X. Wang, H. Pan, *J. Mater. Chem. A* 8 (2020) 23202–23230.
- [54] M. Shao, Y. Shao, S. Ding, R. Tong, X. Zhong, L. Yao, W. Ip, B. Xu, X. Shi, Y. Sun, *ACS Sustain. Chem. Eng.* 7 (2019) 4220–4229.
- [55] W. Li, F. Wang, Y. Shi, L. Yu, *Chin. Chem. Lett.* 34 (2023), 107505.
- [56] X. Deng, R. Qian, H. Zhou, L. Yu, *Chin. Chem. Lett.* 32 (2021) 1029–1032.
- [57] M. Zhou, L. Jing, M. Dong, Y. Lan, Y. Xu, W. Wei, D. Wang, Z. Xue, D. Jiang, J. Xie, *Chemosphere* 268 (2021), 128839.
- [58] R.S. Sahu, Y. Shih, W. Chen, *J. Hazard. Mater.* 402 (2021), 123509.